10560 *Biochemistry* **2003,** *42,* 10560−10568

Articles

Structure and Catalytic Mechanism of L-Rhamnulose-1-phosphate Aldolase[†,‡]

Markus Kroemer, Iris Merkel, and Georg E. Schulz*

Institut für Organische Chemie und Biochemie, Albertstrasse 21, 79104 Freiburg im Breisgau, Germany

Received May 29, 2003; Revised Manuscript Received July 16, 2003

ABSTRACT: The structure of L-rhamnulose-1-phosphate aldolase has been established at 1.35 Å resolution in a crystal form that was obtained by a surface mutation and has one subunit of the C_4-symmetric tetramer in the asymmetric unit. It confirms an earlier 2.7 Å resolution structure which was determined in a complicated crystal form with 20 subunits per asymmetric unit. The chain fold and the active center are similar to those of L-fuculose-1-phosphate aldolase and L-ribulose-5-phosphate 4-epimerase. The active center similarity is supported by a structural comparison of all three enzymes and by the binding mode of the inhibitor phosphoglycolohydroxamate at the site of the product dihydroxyacetone phosphate for the two aldolases. The sensitivity of the catalytic rate to several mutations and a comparison with the established mechanism of the related aldolase give rise to a putative catalytic mechanism. This mechanism involves the same binding mode of the second product L-lactaldehyde in both aldolases, except for a 180° flip of the aldehyde group distinguishing between the two epimers rhamnulose and fuculose. The N-terminal domain exhibits a correlated anisotropic mobility that channels the isotropic Brownian motion into a directed movement of the catalytic base and the substrate phosphate on the N-domain toward the zinc ion and the lactaldehyde on the C-terminal domain. We suggest that this movement supports the catalysis mechanically.

Aldolases are typical enzymes in metabolic pathways of sugars, amino acids, and hydroxy acids. They split into two classes with different reaction mechanisms. Class I aldolases activate the substrate by forming a Schiff base intermediate between a substrate carbonyl carbon and an essential lysine residue, whereas class II aldolases use a divalent metal ion as an electron sink for the aldol cleavage/addition reaction (*1*). Numerous structures of class I aldolases (*2*, *3*) and five structures of class II aldolases (*4*−*9*) have been established. Most of them are homo-oligomers and contain a $(\beta\alpha)_8$-barrel as the common structural motif. The chain folds of the class II enzymes L-fuculose-1-phosphate aldolase (FucA,[1] EC 4.1.2.17) and L-rhamnulose-1-phosphate aldolase (RhuA, EC 4.1.2.19), however, differ greatly from the others, showing an α/β-fold and assembling as a rare C_4-symmetric tetramer. L-Ribulose-5-phosphate 4-epimerase (RibE, EC 5.1.3.4) has been found to be structurally and functionally related to FucA and RhuA (*4*, *10*−*13*).

L-Rhamnose (6-deoxy-L-mannose) is a common component of various glycosides, polysaccharides, and glycoproteins in bacteria and plants. Its uptake and metabolism are performed by proteins encoded in the rhamnose regulon (*14*). Among them, RhuA catalyzes the cleavage of L-rhamnulose-1-phosphate to dihydroxyacetone phosphate (DHAP) and L-lactaldehyde (Figure 1). In the reverse direction, this reaction can be used for carbon−carbon bond formation, creating two new stereo centers. Such enzyme-catalyzed reactions are attractive because they can be applied for the synthesis of chiral compounds (*15*−*17*). In the aldol addition reaction, RhuA accepts a wide range of aldehydes but is highly specific for DHAP (*18*). It is inhibited by phosphoglycolohydroxamate (PGH) which mimics DHAP (*18*, *19*). RhuA is a homotetramer consisting of 274 amino acid residues with an M_r of 30 149 per subunit (*9*, *14*, *20*). Here we report its high-resolution structure and compare it with related enzymes. Moreover, we report the anisotropic mobility of the polypeptide revealed by the high-resolution crystal structure and the activity of several mutants which result in a proposal for the catalytic mechanism.

MATERIALS AND METHODS

Mutagenesis, Protein Purification, Enzyme Activity, and Crystallization. Mutations were performed in the pKK223-3 expression vector using the PCR-based Quikchange kit (Stratagene). Primer 5′-GCCCGGCACGGAC$\underline{\text{GCA}}$ATCG-GCCAGGC-3′ for the successful crystal mutant E192A and the primers for the other mutants together with their antisense partners were obtained from MWG-Biotech (Munich, Germany). All mutations were verified by DNA sequence analyses using the BioCycle kit (GATC, Konstanz, Germany)

[†] This project was supported by Deutsche Forschungsgemeinschaft grant SFB-388.

[‡] The coordinates and structure factors have been deposited in the Protein Data Bank as entry 1OJR.

* To whom correspondence should be addressed: Institut für Organische Chemie und Biochemie, Albertstr. 21, D-79104 Freiburg im Breisgau, Germany. Telephone: +49-761-203-6058. Fax: +49-761-203-6161. E-mail: schulz@bio.chemie.uni-freiburg.de.

[1] Abbreviations: DHAP, dihydroxyacetone phosphate; FucA, L-fuculose-1-phosphate aldolase; PGH, phosphoglycolohydroxamate; RhuA, L-rhamnulose-1-phosphate aldolase; RibE, L-ribulose-5-phosphate 4-epimerase.

10.1021/bi0349266 CCC: $25.00 © 2003 American Chemical Society
Published on Web 08/16/2003

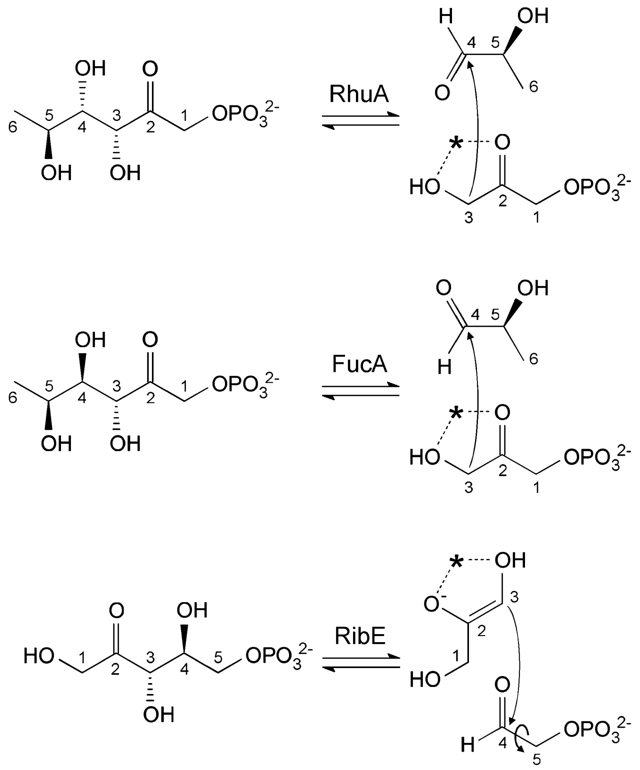

FIGURE 1: Reversible aldol cleavage/addition reactions catalyzed by RhuA, FucA, and RibE. The keto and hydroxyl groups at positions 2 and 3 of the educts L-rhamnulose-1-phosphate, L-fuculose-1-phosphate, and L-ribulose 5-phosphate are aligned because they bind to the Zn^{2+}. The Zn^{2+} ions (∗) are also aligned for the products. The phosphates bind at equivalent polypeptide sites. The two aldolases catalyze the same reaction except for using the respective 4-epimer. In our standard view, DHAP is "below" L-lactaldehyde. For RibE, the glycolaldehyde phosphate is below the dihydroxyacetone moiety and only the first reaction intermediate is shown. The RibE reaction proceeds by a 180° flip of the aldehyde group and a re-addition to yield the 4-epimer D-xylulose 5-phosphate.

or other methods (SeqLab, Göttingen, Germany). The enzyme was produced in *Escherichia coli* JM105 and purified as described previously (*9*). The enzyme activity was determined as with FucA (*21*) except for using L-rhamnulose-1-phosphate instead of its fuculose epimer. Initial crystallization conditions for the mutants were found by screening (*22*). The E192A crystal used for data collection grew under condition 4 of Crystal Screen 2 (Hampton Research, Laguna Niguel, CA) from an 18% (v/v) dioxane solution. A measurement showed a pH of 4.0. For data collection, 20% glycerol was added and the crystal was mounted on a loop and flash-frozen at 100 K. Under exactly defined conditions, it was only possible to reproduce the crystallization of E192A with a buffer of 20 mM potassium phosphate (pH 3.0) and 35% (v/v) dioxane as the reservoir and a 1:1 mixture of this buffer with a 10 mg/mL enzyme solution as the hanging drop.

Data Collection, Molecular Replacement, and Refinement. X-ray diffraction data were collected at 100 K using beamline BW7B (EMBL Outstation, Hamburg, Germany) equipped with an image plate (Marresearch, model 345). Data were processed using MOSFLM (*23*), SCALA (*23*), and TRUNCATE (*23*). The phases were established by molecular replacement using one subunit of the wild-type model (PDB entry 1GT7) without water or PGH (*9*) with AMoRe (*23*). A search in the Patterson range of 2−25 Å performed in the resolution range of 12−5 Å yielded a clear solution, which was subsequently subjected to a rigid-body refinement. The refinement was continued using REFMAC with the bulk-solvent correction (*24*). Model adjustments were made with O (*25*). Water molecules were introduced using ARP (*26*). When the *R*-factor reached ∼20%, double conformations for several side chains, anisotropic *B*-factors, and hydrogen atoms were introduced (*24*). The refinement result was checked in a second anisotropic refinement using SHELX (*27*), which did not reveal discrepancies. The structure alignments were carried out using LSQMAN (*28*). The figures were produced with MOLSCRIPT (*29*) and RASTER3D (*30*).

Table 1: Data Collection and Molecular Replacement[a]

resolution range (Å)	30.5−1.35 (1.40−1.35)
no. of unique reflections	71387 (7660)
completeness (%)	96 (95)
multiplicity	3.7 (3.4)
I/σ_I	8.7 (1.7)
R_{sym} (%)	5.2 (38)
molecular replacement	
rotation, best [second best] correlation coefficient	0.23 [0.16]
translation, best [second best] correlation coefficient	0.65 [0.39]
translation, best [second best] *R*-factor	0.39 [0.48]

[a] The crystals of mutant E192A belonged to space group $P42_12$ and contained one subunit per asymmetric unit with the following unit cell dimensions: $a = b = 108.0$ Å and $c = 57.2$ Å. The data were collected from one crystal at 100 K using a wavelength of 0.8468 Å. Data for the outermost shell are given in parentheses. The second best solutions in molecular replacement are in brackets.

RESULTS AND DISCUSSION

Protein Structure. Crystals of the wild-type enzyme with their 20 crystallographically asymmetric subunits diffracted to only 2.7 Å resolution and were much too complex for a convenient analysis of structural modifications (*9*). For both reasons, we tried to obtain a more suitable crystal form by producing the six point mutants W8T, Q51R, Q52E, D98Y, E192A, and E254R at the protein surface far away from the active center (*31*). All of them yielded crystals, among which those of mutant E192A exhibited superior quality. Data were collected from one E192A crystal (Table 1). The phases were derived by molecular replacement using the model established with the wild-type crystals (*9*). The rotational and the following translational searches yielded a clear solution far above the second best solution (Table 1) which was then taken to be the starting position for the refinement.

Because of the high resolution, every non-hydrogen protein atom was restrained by ∼33 observables (Table 2). Accordingly, the refinement was extended to anisotropic *B*-factors and 23 double side chain conformations. The resulting model was of high quality as the final *R*-factors were low and the backbone dihedral angles were concentrated in the most favorable regions (*32*). Only Arg28 at the tetramer interface near the active center was in a generously allowed region (*32*) as observed with the wild-type structure (*9*). The E192A structure resembled closely that of the wild type; the rmsd of the C_α atoms was merely 0.4 Å. The deviations reached 1.4 Å at residue 52 which is located in packing contacts in both crystal forms (see below). The chain fold is depicted in Figure 2. A closer inspection revealed that the $\beta5-\alpha4-$

Table 2: Refinement Statistics

resolution range (Å)	30.5−1.35
R-factor	0.111
R_{free} (test set of 3.1%)	0.142
no. of non-H atoms (partial occupancy)	
protein[a]	2120
zinc	1
dihydroxyacetone[b]	6 (50%)
phosphate[b]	10 (50%)
active center water[b]	5 (50%)
active center glycerol	6
further glycerol[b]	18 (70−90%)
further water	520
average isotropic *B*-factor[c] (Å^2)	
main chain	12
side chain	14
zinc	9
nonprotein ligands	26
water molecules	34
rmsd for bond lengths (Å) and bond angles (deg)	0.007 and 1.25
Ramachandran regions[d]	
most favorable/allowed (%)	91/9

[a] Double conformations were refined for 23 side chains (20 solvent-accessible and three buried), 15 of which were lysines, glutamines, glutamates, and methionines. The ratios of the partial occupancies ranged between 1:4 and 1:1. [b] Occupancies are given in parentheses. [c] The distribution of the anisotropy values ($U_{\max} - U_{\min}$)/$U_{\max}$ approximates a Gaussian at 0.48 with a σ of 0.13, thus validating the refinement procedure (*38*). $U_{\min}$ and $U_{\max}$ are the shortest and longest axes, respectively, of the displacement tensors describing the *B*-factor anisotropy. [d] Arg28 was in the generously allowed region (*32*) as in the wild-type structure (*9*).

β6 connection is left-handed and that it splits the β-sheet in two parts, $\beta1-\beta5$ and $\beta6-\beta9$. This is a typical topological switch dividing the subunit into two folding units or domains. Because of its intimate contacts, helix α4 was assigned to the C-terminal domain (residues 118−274). The N-domain (residues 1−117) harbors the phosphate binding site and the putative acid/base catalyst Glu117 (see below), whereas the C-domain provides the histidines accommodating the Zn^{2+} ion.

The isotropic *B*-factor distribution in Figure 3 revealed a generally more mobile N-domain with an average of 15 Å^2 (all protein atoms) compared to a value of 12 Å^2 for the C-domain. A similar difference has been found for the respective domains of FucA (*33*) and RibE (*12*). This fits the observation that the C-domain forms the tetramer interface and the N-domain the large protrusion in these enzymes (Figure 2B). The obtained 1.35 Å resolution permitted an anisotropic *B*-factor refinement that revealed a further difference between the N- and C-domains as described in the legend of Figure 3. While the directions of the displacement ellipsoids of the C-domain were randomly distributed, those of the N-domain tended to be azimuthally ordered around the molecular 4-fold axis, indicating a rotational mobility around this axis. Such a rotational displacement pushed the N-domain with its acid/base catalyst Glu117 and substrate phosphate toward the Zn^{2+} ion and the lactaldehyde on the C-domain, supporting the reaction mechanically. We therefore suggest that the correlated anisotropic mobility converts the disordered thermal motion into a directed movement, facilitating catalysis.

A RhuA subunit undergoes numerous contacts. Each of the four tetramer interfaces buries 1340 Å^2 from each of residue sets A and B (Table 3). This adds up to 10720 Å^2 on tetramerization which is 22% of the total surface and therefore in the usual range. The crystal packing contacts affecting residue sets C−F amount to 3920 Å^2 per tetramer, which is 11% and also common. The E192A mutation concerns packing contact set C and was obviously essential for the new crystal form. Notably, half of the residues with double conformations were found in the artificial environment of crystal packing contacts. The packing of the wild-type crystals is much more complex, and only the recurring association into octamers is stated in Table 3.

Structure Comparisons. For a long time, RhuA was thought to be closely related to FucA because the reactions differ only marginally (*16*). However, RhuA has 59 more amino acid residues than FucA, and sequence homology is only revealed if the key residues are taken into account. The similarity between FucA and RibE had been detected in a sequence search accompanying the structure analysis of FucA (*4*) and later analyzed in detail when the structure of RibE was established (*12*, *13*). RibE catalyzes the 4-epimerization of a 2-ketose phosphate which differs chemically from the more common 3-epimerization (*34*) because it is not facilitated by an adjacent keto group (Figure 1). Meanwhile, it has been demonstrated that this reaction runs through an aldol intermediate (*10*−*13*). Moreover, the structural comparison revealed related side chain ligands for Zn^{2+} and phosphate that constitute the two anchor points of substrate binding.

A superposition of the three structurally known family members resulted in quite a number of large gaps (Figure 4). An evaluation showed that the subunits of RhuA and FucA can be superimposed on 136 C_α atoms within the usual 3 Å cutoff (Table 4). When the tetramers were superimposed, this number dropped to 80 per subunit. The comparison between RhuA and RibE resulted in a lower level of similarity, indicating a more distant relationship than between the aldolases. Moreover, the superposition of FucA with RibE revealed a much closer relationship than between any one of them and RhuA. Within the family, the level of sequence identity in the structure-aligned part shows the same relationship as the chain folds (Table 4). Nine of the 15 conserved residues of Figure 4 outline the Zn^{2+} and phosphate sites. The other six residues exhibit varying degrees of conservation in a comparison of all known RhuA, FucA, and RibE sequences (data not shown), starting from the best conserved His121 via Glu232, Gly101, Ala235, and Leu208 to the least conserved Glu192.

The five N-terminal insertions in RhuA enlargen the protrusion at the bottom end of Figure 2, indicating a great evolutionary distance. Moreover, the C-termini of FucA and RibE are disordered, while the respective residues after helix α10 of RhuA (Figure 4) are rigid. In both FucA and RibE, some of these disordered residues are important for the catalytic reaction (*11*−*13*, *19*, *21*), presumably because they cover and interact with the bound substrate (*21*, *35*). Now in RhuA, we find that the corresponding residues cannot contribute directly to catalysis as they run away from the active center. Since they exhibit low *B*-factors and are identical in the two crystal forms and not in a packing contact, their location is most likely natural.

Substrate Binding. The structure refinement resulted in three regions of clear residual density at the active center that could not be explained by water molecules (Figure 5A).

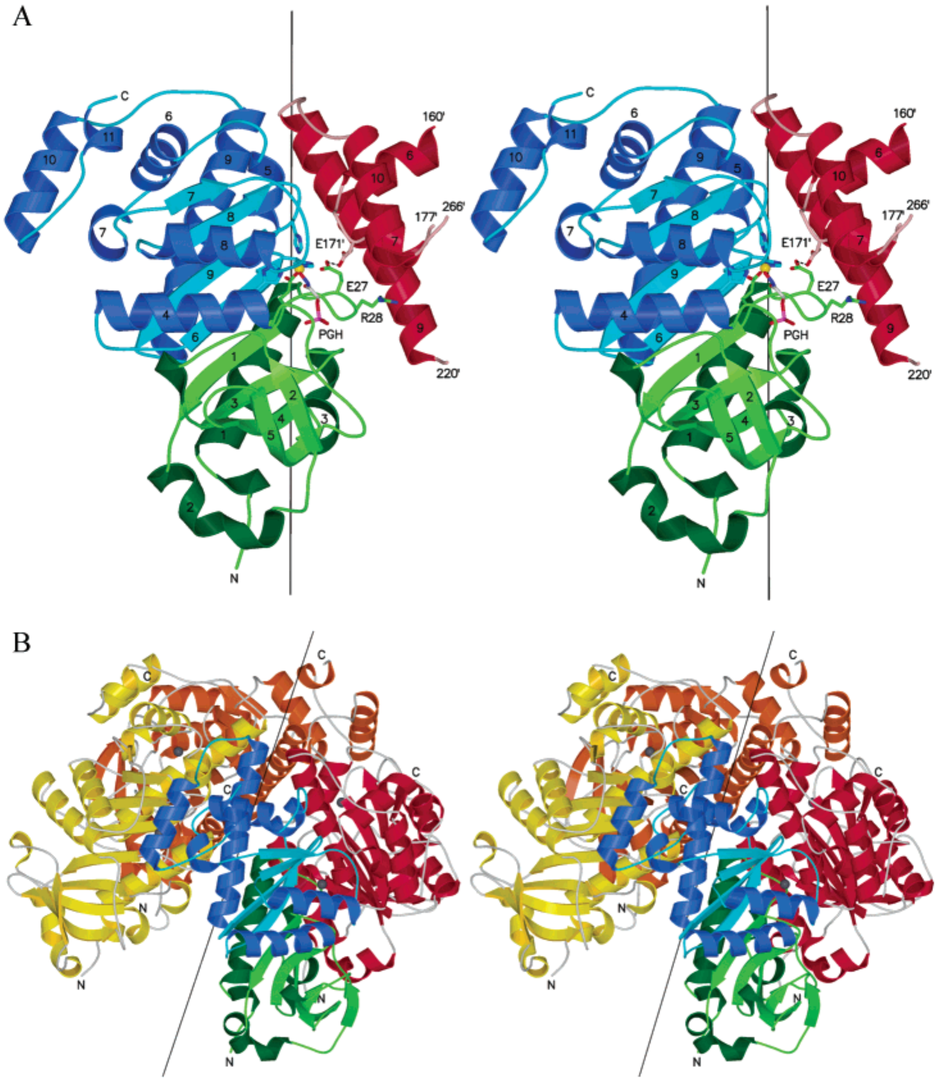

FIGURE 2: Stereoview of RhuA. (A) Ribbon plot of one subunit including the peptide of the neighboring subunit that participates in the active center (red). The N-terminal domain is green, and the C-terminal domain after the topology switch is blue. The Zn^{2+} ion, its histidine ligands, Glu117, and PGH are shown. Residues 27, 28, and 171′ at the interface are depicted in their conformations observed at low pH in both crystal structures. (B) Ribbon plot of a tetramer showing the molecular 4-fold axis and emphasizing that the N-domain protrudes from the bulk.

Table 3: Contacts Formed by One Subunit of RhuA

contact	name of residue set[a]	contact area[b] (Å^2)	set of affected residues
interface	A	1340	21, 22, 24, 27−30, 78, 80, 81, 84, 143, 145, 146, 148−156, 185, 187−190, 211, 212, 236, 239, 242, 243
interface	B	1340	15, 19, 22, 23, 167−171, 174, 175, 222, 223, 225−227, 229, 230, 233, 236−238, 240, 241, 243, 244, 246−251, 255, 258, 259, 262, 263
E192A packing	C	460	59−61, 63, 100, 127, 130, 183, 184, 186, 191, 192, 195, 196, 199, 200, 202, 203
E192A packing	D	420	46, 47, 51−55, 97, 98, 103
E192A packing	E	50	1, 2
E192A packing	F	50	155
wild-type octamer[c]	G	400	1, 2, 6, 8, 11, 40, 41, 43−45, 220, 222
wild-type octamer[c]	H	350	1, 3, 46−48, 51, 52, 84, 85, 109−111

[a] The following contact pairs are formed: A−B, C−C′, D−D′, E−F, G−G′, and H−H′. [b] The contact area is half of the buried solvent-accessible area of both partners. [c] In the wild-type crystal (*9*), all five crystallographically independent tetramers use the G−G′ and H−H′ contacts to form octamers.

One of the density regions was fitted by a fully occupied glycerol from the cryoprotection buffer. A second density region at the Zn^{2+} was interpreted as a superposition of 50% occupied dihydroxyacetone and 50% phosphate. Dihydroxyacetone was a 0.2% impurity in the cryoprotectant glycerol as shown by a spectrophotometric analysis. The phosphate was from the last purification buffer and had escaped dialysis (*9*). Phosphates bound to Zn^{2+} have been found (*36*). The third density region is at the phosphate site and has been assigned to a 50% occupied phosphate and five water molecules associated with the remaining 50% of the molecules.

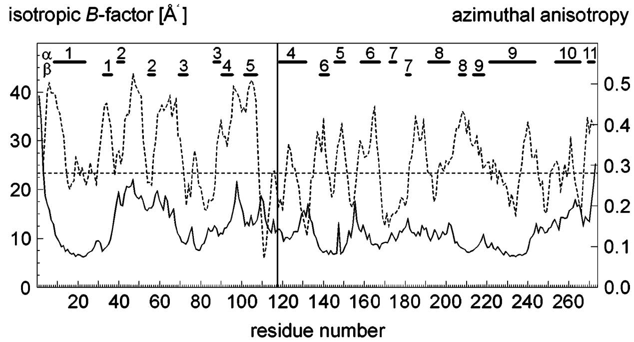

FIGURE 3: Polypeptide mobility of the 1.35 Å resolution E192A crystal structure represented by the isotropic *B*-factors of the C_α atoms (—). The division between N- and C-domains is indicated by a vertical line. The averages in these two domains are 15 and 12 $Å^2$, respectively. The *B*-factor distribution of the 2.7 Å resolution wild-type crystal structure shows peaks at the same position, but all values are ~3 times higher. The scale at the right-hand side refers to the anisotropic *B*-factors of all C_α atoms, which were converted to vectors in the direction of $U_{\max}$ with lengths $(U_{\max} - U_{\min})/U_{\max}$, where $U_{\max}$ and $U_{\min}$ are the longest and shortest axes, respectively, of the anisotropic displacement tensors. These vectors were represented in cylindrical coordinates around the molecular 4-fold axis. Their azimuthal components, i.e., the rotational freedom around the molecular 4-fold axis, are displayed as a dotted line. Note that the vector length distribution approximates a Gaussian with an average of 0.48 and a standard deviation of 0.13 (Table 2) as commonly observed (*38*); therefore, the average length of each component is $0.48 \times 3^{-1/2}$ (0.28), as indicated by a horizontal dotted line. A single component reaches a value of 0.48 if the vector points in its direction. Accordingly, the vector points predominantly along the azimuthal component in the N-domain but shows no directional preference in the C-domain. As a consequence, the anisotropic displacement of the N-domain corresponds to a rotational movement around the molecular 4-fold axis.

Table 4: Structure and Sequence Comparisons[a]

	RhuA	FucA	RibE
RhuA	−	136 (1.4 Å) 4 × 80 (1.7 Å)	127 (1.6 Å) 4 × 46 (1.8 Å)
FucA	18%	−	168 (1.3 Å) 4 × 123 (1.6 Å)
RibE	14%	25%	−

[a] The bottom left triangle shows the percentage of identical residues in the structure-based alignment of Figure 4. The top right triangle gives the number of residues aligned in C_α backbone comparisons using LSQMAN (*28*) with a 3 Å cutoff. The respective upper lines contain the residue numbers for the superposition of a single subunit, whereas the lower lines refer to superpositions of the tetramers. The resulting rmsd values are given in parentheses.

These interpretations explain the data well. They outline the phosphate site and the available space for a zinc ligand. In a later structure analysis of an E192A crystal that had been grown from the phosphate buffer specified above, two phosphates at approximately full occupancy were observed: one at the phosphate site and the other at the Zn^{2+}. The data were much lower in quality and therefore not further pursued. The electron density and the binding structure of PGH with wild-type RhuA are shown in Figure 5B. The split in the density distribution at the depicted high contour level indicates the predominance of the two anchor points at the Zn^{2+} and at the phosphate site, allowing motions in the region between them. A superposition of the E192A and wild-type crystal structures in Figure 5C showed displacements of Arg28 and Leu173 but almost no other changes.

The analysis of FucA resulted in detailed proposals for the binding modes of L-fuculose-1-phosphate and for the reaction mechanism as it is sketched in Figure 1 (*19*, *21*, *35*). The aldol cleavage reactions of RhuA and FucA produce DHAP binding tightly to Zn^{2+} and the phosphate site (Figure 5B) and an L-lactaldehyde that finds no obvious anchor site, in agreement with the lower specificity for this moiety (*16*).

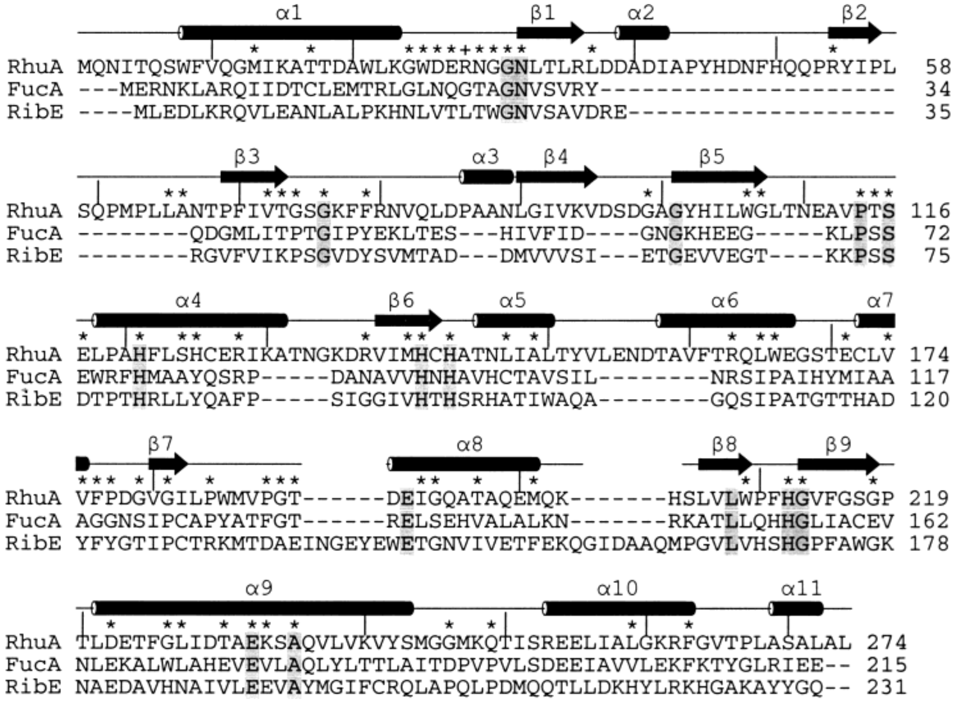

FIGURE 4: Structure-based sequence alignment of aldolases RhuA and FucA with the 4-epimerase RibE. All enzymes are from *E. coli*. The secondary structures are from RhuA. The 15 conserved residues in sequence and space are emphasized by shading. The strictly conserved residues in the eight established RhuA sequences under codes P32169, Q8ZKS1, Q8ZJ03, Q8Y3I8, Q926R2, AAO80291, Q8ESW9, and Q88S52 (*39*) with mutual levels of sequence identity between 37 and 91% are marked (∗). The (+) mark for Arg28 means that one of the eight sequences contains a leucine (one base exchange) at this position.

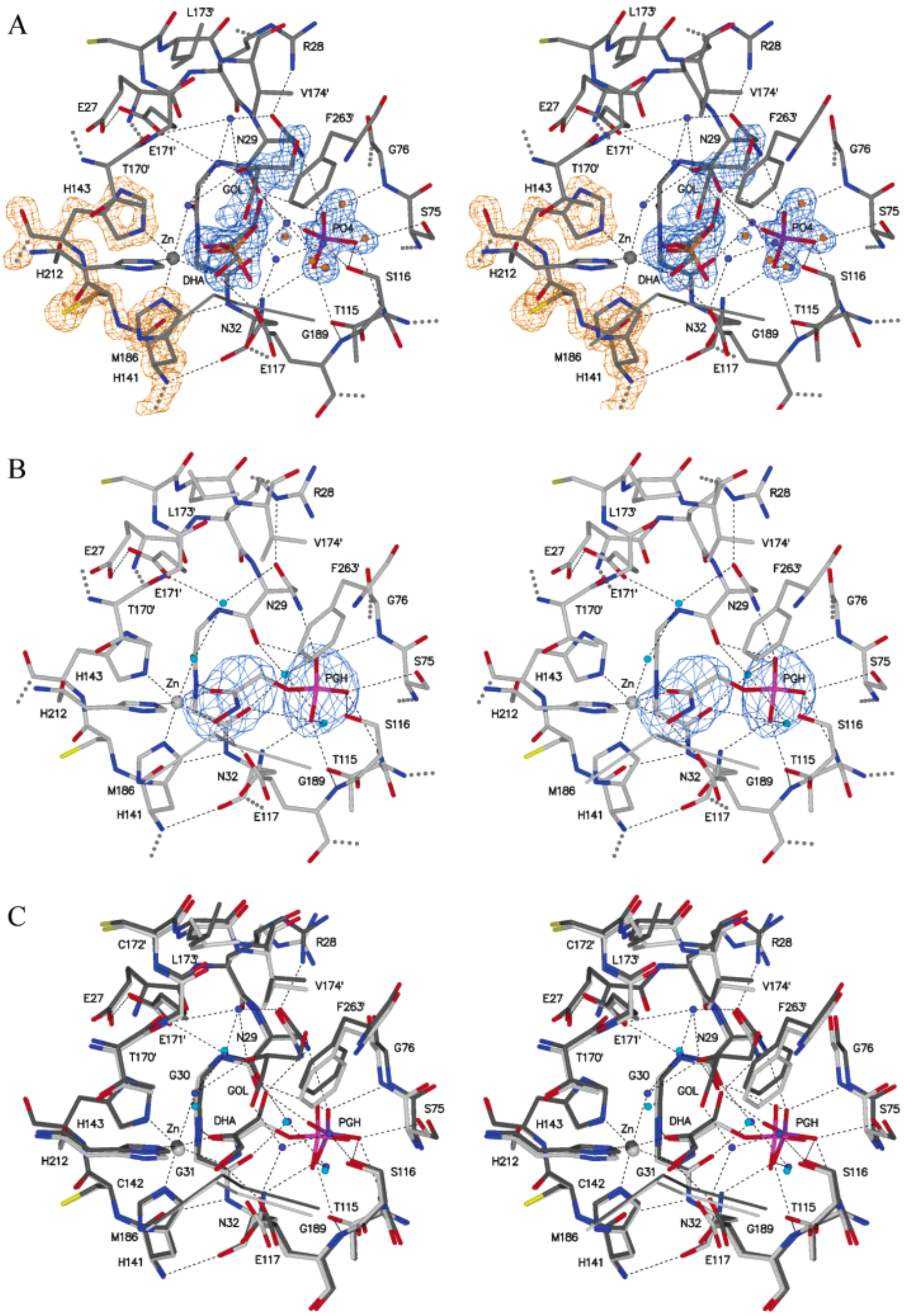

FIGURE 5: Stereoview of the active center of RhuA. (A) High-resolution E192A structure with the simulated annealed $F_o - F_c$ difference density for the ligands at the 4.5σ level (blue). The ligands are glycerol (100% occupied), dihydroxyacetone (50%), phosphate at Zn^{2+} (50%), phosphate (50%), and five water molecules at the phosphate site (50%) (Table 2). The high quality of the polypeptide structure is demonstrated by the final $2F_o - F_c$ electron density shown for two zinc-liganding histidines and a cysteine at the 3.3σ level (orange). (B) Medium-resolution wild-type structure with PGH showing the simulated annealed $F_o - F_c$ difference density at the 4.5σ level. The density distribution is continuous at the 3.6σ level. (C) Superposition of the E192A (dark gray) and wild-type (light gray) structures, where the only peptide differences occur at Arg28 and Leu173.

As a consequence, the bound aldehyde moiety had to be modeled in FucA (Figure 6A), and a similar modeling procedure is now required for RhuA.

The superposition of the active centers of FucA and RhuA in Figure 6A shows a well-conserved PGH, revealing the binding mode of DHAP. In the aldol addition reaction, the DHAP 3-carbanion has to attack the *si* face of the aldehyde group in FucA or the *re* face of this group in RhuA (Figure 1). Since the F131A mutation of FucA, which provides space at the left-hand side of the aldehyde in Figure 6A, caused the FucA mutant to produce the rhamnulose instead of the fuculose epimer from the nonpolar propion- and isobutyraldehydes (*21*), it was suggested that aldehyde binding to RhuA is related by a 180° rotation around the C4−O4 bond to the binding mode in FucA (see Figure 1). However, RhuA has no space at the left-hand side and cannot accommodate the O4 atom at the same position as in FucA as it contains no hydrogen bonding residue equivalent to Tyr113′ of FucA. Therefore, we suggest that the aldehyde bound to RhuA differs from that in FucA by a 180° rotation around the C4−

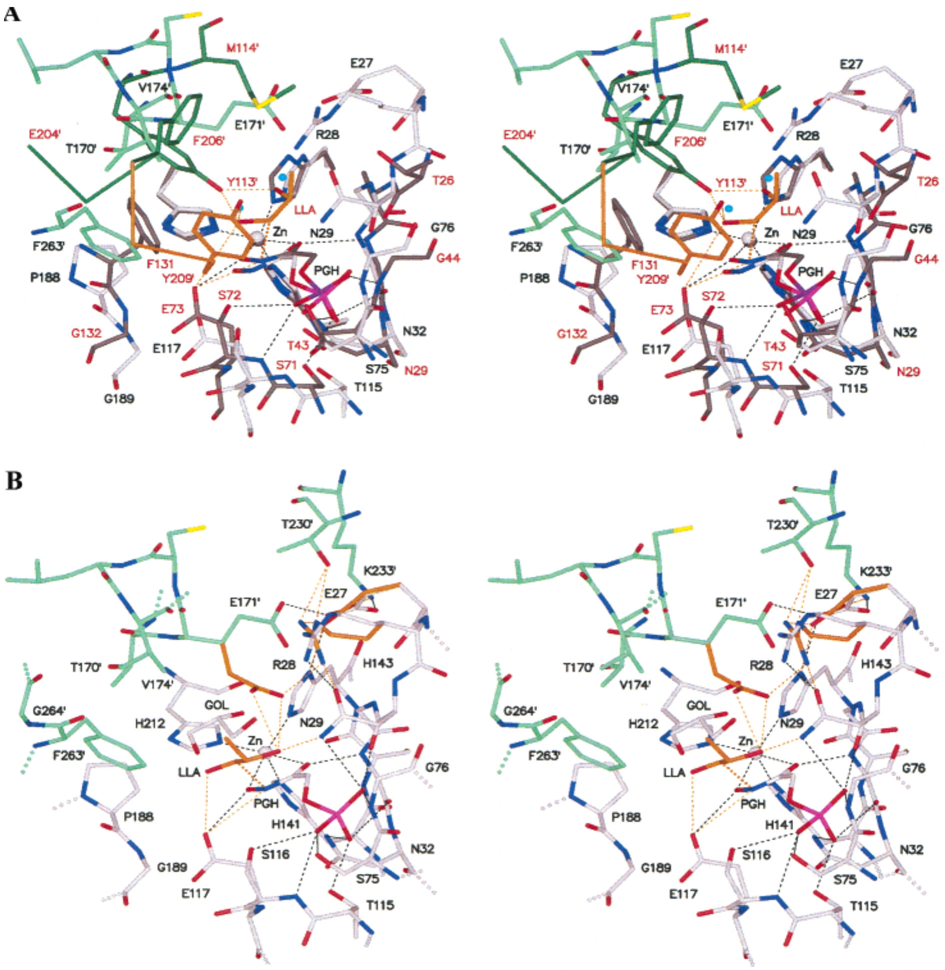

FIGURE 6: Active center and catalytic mechanism. (A) Superposition of the active centers of RhuA (light colors) and FucA (dark colors) as based on the Zn^{2+} with its three histidines and PGH. Residues from the neighboring subunit are green. The modeled L-lactaldehyde (LLA) and the modeled catalytically important though disordered residue Tyr209′ of FucA (*21*, *35*) are shown in orange. (B) Active center of RhuA showing the bound glycerol (GOL) and the strong hydrogen bond between Glu171′ and Glu27 that depends on the low pH values of 4.6 and 4.0 in the wild-type and E192A crystals, respectively. The modeled L-lactaldehyde and the modeled Glu27, Arg28, and Glu171′ arrangement at physiological pH are included in orange. Note that the location of the 4-keto group in RhuA differs from that in FucA, distinguishing between the two epimers.

C5 bond as it is sketched in Figure 1. This allows Glu117 to de- and reprotonate atoms O4 and C3, as performed by the equivalent Glu73 of FucA. Moreover, it brings the methyl group of the aldehyde into a hydrophobic environment that is outlined by the carbon backbone of the bound glycerol (Figure 6B). We conclude that the F131A mutation converting FucA into a RhuA for nonpolar aldehydes (*21*) resulted in a reaction geometry differing from that of natural RhuA.

In contrast to FucA and RhuA, no substrate analogue could be bound to crystalline RibE, yet the Zn^{2+} position was clear and the phosphate site suggested by the homology with FucA (*12*, *13*). These two anchors and the known effects of numerous mutants and isotopes on the activity suggested the reaction geometry sketched in Figure 1 (*10*−*13*). After C−C bond cleavage, the 4-epimerization involves a 180° rotation of the aldehyde group and a C−C re-addition to yield the 4-epimer. Asp120 and Tyr229 of RibE are likely to de- and reprotonate the O4 atom as suggested by the immense activity decrease on mutation (*13*). In contrast, Asp76 of RibE which aligns with catalyst Glu117 of RhuA (Figure 4) is of little importance (*13*). The binding model implies a strong fixation of the dihydroxyacetone at the Zn^{2+} and of the aldehyde at the phosphate site so that the split in the middle and the aldehyde flip are not detrimental to the binding strength.

Table 5: Enzyme Kinetics[a]

	activity (%)	k_{cat}/K_M (%)		activity (%)	k_{cat}/K_M (%)
wild type	100	100	N29A	4	0.9
E192A	100	100	E171S	2	0.7
G264Stop	75	78	E171A	0.4	0.3
R28A	23	7	E171Q	0.4	0.1
R28S	9	2	E117Q	0.1	0.04

[a] The activity has been measured using 2.4 mM L-rhamnulose-1-phosphate in a coupled assay (*21*) at 37 °C with 9.8 μg of RhuA (wild type) per milliliter. The specific activity of the wild type was 20 units/mg. The wild-type K_M value was 0.48 mM. The differences between the activities and the k_{cat}/K_M values show that the K_M values increased appreciably on mutation of substrate binding residues Arg28 and Asn29 (Figure 6B).

Enzyme Kinetics and Reaction Mechanism. The substrate binding model of Figure 6B was compared with the kinetic data of several mutants given in Table 5. First of all, mutant E192A was indistinguishable from the wild type, confirming that this mutation affected only the crystallization and that its conservation (Figure 4) is a coincidence. Although we observed the C-terminal residues of RhuA in a fixed conformation away from the active center and away from any packing contact (Table 3), the disordered conformations and the importance of the equivalent parts of FucA (*4*, *21*) and RibE (*12*, *13*) recommended a check. Therefore, we deleted residues 264−274 in mutant G264Stop but found no dramatic activity decrease (Table 5). Consequently, RhuA differs from the two other enzymes by lacking a mobile peptide segment with catalytic competence, confirming the great evolutionary distance already detected in the alignment (Figure 4).

Next we checked the importance of Arg28 with its unfavorable backbone dihedral angles by introducing two mutations. Both resulted in remarkable activity decreases, partially caused by a K_M increase corresponding to a diminished binding strength. The activity dropped further when mutating Asn29 which contacts the phosphate and presumably also the 5-hydroxyl group of the substrate. As a surprise, the activity was even more strongly affected by mutation of Glu171 that points away from the active center in both crystal structures. The lowest activity of all, however, was measured upon mutation of Glu117 that is proposed to de- and reprotonate the O4 and C3 atoms of the substrate during the reaction. This confirmed the catalytic role of Glu117 and thus the position of the O4 atom in our model (Figure 6B).

On first sight, the strong effect of the three Glu171 mutations appeared to contradict our substrate binding model. However, the two crystal forms were at pH values of 4.0 and 4.6 so that Glu171′ from the neighboring subunit was drawn into a strong hydrogen bond with Glu27 as depicted in Figures 2 and 6B. At pH 7, however, both glutamates are charged and repel each other so that Arg28 is likely to connect the two carboxylates as modeled in Figure 6B. At its physiological position, Glu171′ fixes the 5-hydroxyl and thus the aldehyde, explaining its importance for the catalysis. This proposal is supported by the strong conservation of Glu27, Arg28, and Glu171 within the RhuA family (Figure 4). At the modeled position, Glu171′ can also act as a general acid/base catalyst for the opening of the predominant ring form (*37*) of L-rhamnulose-1-phosphate because it can protonate the ring oxygen and bind the resulting 5-hydroxyl.

After clarifying the substrate positions, we suggest that the aldol cleavage reaction proceeds in the following sequence. The ring form of L-rhamnulose-1-phosphate is opened by Glu171′, and the resulting open form binds to the enzyme forming a diolate at the Zn^{2+}. Glu117 abstracts a proton from O4, causing the split of the C3−C4 bond and the formation of a C3 carbanion, which is subsequently protonated by Glu117. The products L-lactaldehyde and DHAP dissociate. It has been suggested (*19*) that the aldol cleavage/addition reaction of FucA is energetically supported by the motion of the N-domain relative to the C-domain that manifests itself in the higher *B*-factors of the protruding N-domain with respect to the tetramer-forming C-domain. This proposal has now been refined because the high-resolution structure of RhuA revealed a correlated anisotropic mobility of the N-domain that corresponds to a movement of the catalytic acid/base and the substrate phosphate toward the Zn^{2+} ion and the lactaldehyde, i.e., along the cleaved or formed bond of the reaction. We suggest that this movement supports the reaction mechanically.

ACKNOWLEDGMENT

We thank W.-D. Fessner for the RhuA expression plasmid and for a gift of L-rhamnulose-1-phosphate, J. V. Schloss and M. Hixon for a gift of phosphoglycolohydroxamate, and R. Thoma, M. Lucassen, and D. Grüninger for several measurements. Moreover, we are grateful to the team of the EMBL Outstation in Hamburg for their help with the synchrotron data collection.

NOTE ADDED AFTER ASAP POSTING

In the version of this paper published on the Web on 08/16/03, panels A and B of Figure 6 were identical. The correct electronic version of this paper was published on 08/22/03.

REFERENCES

1. Horecker, B. L., Tsolas, O., and Lai, C. Y. (1972) Aldolases, in *The Enzymes* (Boyer, P. D., Ed.) 3rd ed., Vol. 7, pp 213−258, Academic Press, New York.
2. Mavridis, I. M., Hatada, M. H., Tulinsky, A., and Lebioda, L. (1982) Structure of 2-keto-3-deoxy-6-phosphogluconate aldolase at 2.8 Å resolution, *J. Mol. Biol. 162*, 419−444.
3. Sakuraba, H., Tsuge, H., Shimoya, I., Kawakami, R., Goda, S., Kawarabayasi, Y., Katunuma, N., Ago, H., Miyano, M., and Ohshima, T. (2003) The first crystal structure of archaeal aldolase. Unique tetrameric structure of 2-deoxy-D-ribose-5-phosphate aldolase from the hyperthermophilic archaea *Aeropyrum pernix*, *J. Biol. Chem. 278*, 10799−10806.
4. Dreyer, M. K., and Schulz, G. E. (1993) The spatial structure of the class II L-fuculose-1-phosphate aldolase from *Escherichia coli*, *J. Mol. Biol. 231*, 549−553.
5. Blom, N. S., Tétreault, S., Coulombe, R., and Sygusch, J. (1996) Novel active site in *Escherichia coli* fructose 1,6-bisphosphate aldolase, *Nat. Struct. Biol. 3*, 856−862.
6. Cooper, S. J., Leonard, G. A., McSweeney, S. M., Thompson, A. W., Naismith, J. H., Qamar, S., Plater, A., Berry, A., and Hunter, W. N. (1996) The crystal structure of a class II fructose-1,6-bisphosphate aldolase shows a novel binuclear metal-binding active site embedded in a familiar fold, *Structure 4*, 1303−1315.
7. Izard, T., and Blackwell, N. C. (2000) Crystal structures of the metal-dependent 2-dehydro-3-deoxy-galactarate aldolase suggest a novel reaction mechanism, *EMBO J. 19*, 3849−3856.
8. Hall, D. R., Bond, C. S., Leonard, G. A., Watt, C. I., Berry, A., and Hunter, W. N. (2002) Structure of tagatose-1,6-bisphosphate aldolase, *J. Biol. Chem. 277*, 22018−22024.
9. Kroemer, M., and Schulz, G. E. (2002) The structure of L-rhamnulose-1-phosphate aldolase (class II) solved by low-resolution SIR phasing and 20-fold NCS averaging, *Acta Crystallogr. D58*, 824−832.
10. Johnson, A. E., and Tanner, M. E. (1998) Epimerization via carbon−carbon bond cleavage. L-Ribulose-5-phosphate 4-epimerase as a masked class II aldolase, *Biochemistry 37*, 5746−5754.
11. Lee, L. V., Poyner, R. R., Vu, M. V., and Cleland, W. W. (2000) Role of metal ions in the reaction catalyzed by L-ribulose-5-phosphate 4-epimerase, *Biochemistry 39*, 4821−4830.
12. Luo, Y., Samuel, J., Mosimann, S. C., Lee, J. E., Tanner, M. E., and Strynadka, N. C. J. (2001) The structure of L-ribulose-5-phosphate 4-epimerase: An aldolase-like platform for epimerization, *Biochemistry 40*, 14763−14771.
13. Samuel, J., Luo, Y., Morgan, P. M., Strynadka, N. C. J., and Tanner, M. E. (2001) Catalysis and binding in L-ribulose-5-phosphate 4-epimerase: A comparison with L-fuculose-1-phosphate aldolase, *Biochemistry 40*, 14772−14780.
14. Moralejo, P., Egan, S. M., Hidalgo, E., and Aguilar, J. (1993) Sequencing and characterization of a gene cluster encoding the enzymes for L-rhamnose metabolism in *Escherichia coli*, *J. Bacteriol. 175*, 5585−5594.
15. Bednarski, M. D., Simon, E. S., Bischofberger, N., Fessner, W.-D., Kim, M.-J., Lees, W., Saito, T., Waldmann, H., and White-

sides, G. M. (1989) Rabbit muscle aldolase as a catalyst in organic synthesis, *J. Am. Chem. Soc. 111*, 627−635.

16. Fessner, W.-D., Sinerius, G., Schneider, A., Dreyer, M., Schulz, G. E., Badia, J., and Aguilar, J. (1991) Diastereoselective enzymatic aldol additions: L-rhamnulose and L-fuculose-1-phosphate aldolases from *E. coli*, *Angew. Chem., Int. Ed. Engl. 30*, 555−558.
17. Wong, C.-H., Halcomb, R. L., Ichikawa, Y., and Kajimoto, T. (1995) Enzymes in organic synthesis: application to the problems of carbohydrate recognition, *Angew. Chem., Int. Ed. Engl. 34*, 412−432.
18. Fessner, W.-D., Schneider, A., Held, H., Sinerius, G., Walter, C., Hixon, M., and Schloss, J. V. (1996) The mechanism of class II, metal-dependent aldolases, *Angew. Chem., Int. Ed. Engl. 35*, 2219−2221.
19. Dreyer, M. K., and Schulz, G. E. (1996) Catalytic mechanism of the metal-dependent fuculose aldolase from *Escherichia coli* as derived from the structure, *J. Mol. Biol. 259*, 458−466.
20. Sawada, H., and Takagi, Y. (1964) The metabolism of L-rhamnose in *Escherichia coli*, *Biochim. Biophys. Acta 92*, 26−32.
21. Joerger, A. C., Gosse, C., Fessner, W.-D., and Schulz, G. E. (2000) Catalytic action of fuculose 1-phosphate aldolase (class II) as derived from structure-directed mutagenesis, *Biochemistry 39*, 6033−6041.
22. Jancarik, J., and Kim, S.-H. (1991) Sparse matrix sampling: a screening method for crystallization of proteins, *J. Appl. Crystallogr. 24*, 409−411.
23. Collaborative Computational Project, Number 4 (1994) The CCP4 suite: programs for protein crystallography, *Acta Crystallogr. D50*, 760−763.
24. Murshudov, G. N., Vagin, A. A., and Dodson, E. J. (1997) Refinement of macromolecular structures by the maximum-likelihood method, *Acta Crystallogr. D53*, 240−255.
25. Jones, T. A., Zou, J.-Y., Cowan, S. W., and Kjeldgaard, M. (1991) Improved methods for building protein models in electron density maps and the location of errors in these models, *Acta Crystallogr. A47*, 110−119.
26. Lamzin, V. S., and Wilson, K. S. (1993) Automated refinement of protein models, *Acta Crystallogr. D49*, 129−147.
27. Sheldrick, G. M., and Schneider, T. R. (1997) SHELXL: high-resolution refinement, *Methods Enzymol. 277*, 319−343.
28. Kleywegt, G. J. (1996) Use of non-crystallographic symmetry in protein structure refinement, *Acta Crystallogr. D52*, 842−857.
29. Kraulis, P. J. (1991) MOLSCRIPT: A program to produce both detailed and schematic plots of protein structures, *J. Appl. Crystallogr. 24*, 946−950.
30. Merritt, E. A., and Bacon, D. J. (1997) RASTER3D: Photorealistic molecular graphics, *Methods Enzymol. 277*, 505−524.
31. Pautsch, A., Vogt, J., Model, K., Siebold, C., and Schulz, G. E. (1999) Strategy for membrane protein crystallization exemplified with OmpA and OmpX, *Proteins 34*, 167−172.
32. Laskowski, R. A., MacArthur, M. W., Moss, D. S., and Thornton, J. M. (1993) PROCHECK: A program to check the stereochemical quality of protein structures, *J. Appl. Crystallogr. 26*, 283−291.
33. Dreyer, M. K., and Schulz, G. E. (1996) Refined high-resolution structure of the metal-ion dependent L-fuculose-1-phosphate aldolase (class II) from *Escherichia coli*, *Acta Crystallogr. D52*, 1082−1091.
34. Kopp, J., Kopriva, S., Süss, K.-H., and Schulz, G. E. (1999) Structure and mechanism of the amphibolic enzyme D-ribulose-5-phosphate 3-epimerase from potato chloroplasts, *J. Mol. Biol. 287*, 761−771.
35. Joerger, A. C., Mueller-Dieckmann, C., and Schulz, G. E. (2000) Structures of L-fuculose-1-phosphate aldolase mutants outlining motions during catalysis, *J. Mol. Biol. 303*, 531−543.
36. Alberts, I. L., Nadassy, K., and Wodak, S. J. (1998) Analysis of zinc binding sites in protein crystal structures, *Protein Sci. 7*, 1700−1716.
37. Pierce, J., Serianni, A. S., and Barker, R. (1985) Anomerization of furanose sugars and sugar phosphates, *J. Am. Chem. Soc. 107*, 2448−2456.
38. Merritt, E. A. (1999) Expanding the model: anisotropic displacement parameters in protein structure refinement, *Acta Crystallogr. D55*, 1109−1117.
39. Boeckmann, B., Bairoch, A., Apweiler, R., Blatter, M.-C., Estreicher, A., Gasteiger, E., Martin, M. J., Michoud, K., O'Donovan, C., Phan, I., Pilbout, S., and Schneider, M. (2003) The SWISS-PROT protein knowledge base and its supplement TrEMBL in 2003, *Nucleic Acids Res. 31*, 365−370.

BI0349266